Supplemental Material for "Temperature Dependence of the Energy Levels of Methylammonium Lead Iodide Perovskite from First Principles"

Wissam A. Saidi,[*,†] Samuel Poncé,[‡] and Bartomeu Monserrat[¶]

†*Department of Mechanical Engineering and Materials Science, University of Pittsburgh, Pittsburgh 15261, USA*

‡*Department of Materials, University of Oxford, Parks Road, Oxford OX1 3PH, United Kingdom*

¶*Department of Physics and Astronomy, Rutgers University, Piscataway, New Jersey 08854-8019, USA*

§*TCM Group, Cavendish Laboratory, University of Cambridge, J. J. Thomson Avenue, Cambridge CB3 0HE, United Kingdom*

E-mail: alsaidi@pitt.edu

Computational details

Most calculations reported in the main text have been performed using the plane-wave DFT code VASP.[1–4] We use the PBE[5] and HSE[6,7] functionals as described in the text, together with the projector augmented-wave method.[8,9] The energy cut-off used is 500 eV, and the electronic Brillouin zone (BZ) is sampled using a $6 \times 6 \times 6$ grid for the primitive cell, and commensurate grids for the supercells. Spin-orbit coupling (SOC) is included as described in the text.

The vibrational harmonic calculations have been done using the finite displacement method in conjunction with nondiagonal supercells.[10] The electron-phonon coupling calculations using the FD approach have also been performed using the finite displacement approach and nondiagonal supercells. The non-adiabatic Allen-Heine-Cardona calculations based on DFPT have been performed with the ABINIT software[11] using a $6\times6\times6$ $\mathbf{\Gamma}$-centered $\mathbf{k}$-point grid with a plane-wave energy cutoff of 680 eV. Norm-conserving pseudopotential with the PBE functional have been used. The vibrational BZ was sampled using grids of sizes up to $20 \times 20 \times 20$.

The cubic cell that we have used in our calculations exhibits some imaginary phonon frequencies, reflecting the dynamical instability of this structure, and driving it towards the lower-temperature tetragonal and orthorhombic structures. In the calculations reported in the main manuscript, we have set the amplitudes of the vibrational modes corresponding to imaginary frequencies to zero, to be able to work with the cubic structure. We have performed additional calculations for the $2 \times 2 \times 2$ supercell in which we have allowed the imaginary modes to contribute to electron-phonon coupling by describing them using Gaussian vibrational wave functions of amplitude given by the absolute value of their (imaginary) frequencies, in the spirit of the self-consistent harmonic approximation. Our calculations show that the temperature dependence does not change within error bars whether the unstable modes are allowed to contribute or not.

Expansion order in the electron-phonon interaction

The electronic state average over atomic vibrations

$$\epsilon_{\mathbf{k}n}(T) = \frac{1}{\mathcal{Z}} \sum_{\mathbf{s}} \langle \chi_{\mathbf{s}} | \epsilon_{\mathbf{k}n} | \chi_{\mathbf{s}} \rangle e^{-E_{\mathbf{s}}/k_{\mathrm{B}}T}, \tag{1}$$

is usually performed using a *quadratic approximation* to the dependence of $\epsilon_{\mathbf{k}n}$ on the atomic configuration. In terms of normal modes of vibration $u_{\mathbf{q}\nu}$ characterized by a wave vector $\mathbf{q}$ with branch ν, the value of the electronic state at a general atomic configuration $\mathbf{u} = \{u_{\mathbf{q}\nu}\}$ can be expanded around its equilibrium position as

$$\epsilon_{\mathbf{k}n}(\mathbf{u}) = \epsilon_{\mathbf{k}n}(\mathbf{0}) + \sum_{\mathbf{q},\nu} a^{(1)}_{\mathbf{q}\nu} u_{\mathbf{q}\nu} + \sum_{\mathbf{q},\nu,\mathbf{q}',\nu'} a^{(2)}_{\mathbf{q}\nu;\mathbf{q}'\nu'} u^*_{\mathbf{q}\nu} u_{\mathbf{q}'\nu'} + \cdots, \tag{2}$$

where $\{a^{(1)}_{\mathbf{q}\nu}, a^{(2)}_{\mathbf{q}\nu;\mathbf{q}'\nu'}, \ldots\}$ are the electron-phonon coupling constants. Truncating this expansion at second order and substituting into Eq. (1) leads to

$$\Delta\epsilon_{\mathbf{k}n}(T) \triangleq \epsilon_{\mathbf{k}n}(T) - \epsilon_{\mathbf{k}n}(\mathbf{0}) = \frac{1}{N_{\mathbf{q}}} \sum_{\mathbf{q},\nu} \frac{a^{(2)}_{\mathbf{q}\nu;\mathbf{q}\nu}}{\omega_{\mathbf{q}\nu}} \left[\frac{1}{2} + n_{\mathrm{B}}(\omega_{\mathbf{q}\nu}, T) \right], \tag{3}$$

where $\Delta\epsilon_{\mathbf{k}n}(T)$ is the phonon renormalization of the electronic state at temperature T, $N_{\mathbf{q}}$ is the number of points in the vibrational BZ, $\omega_{\mathbf{q}\nu}$ is the harmonic frequencies of mode $(\mathbf{q}, \nu)$, and n_{B} is a Bose-Einstein factor. The expression in Eq. (3) is computationally convenient, as the coupling constants of interest only depend on individual modes, and can be efficiently calculated using density functional perturbation theory (DFPT)[12] or finite displacements.[13]

To obtain a DFPT formulation of Eq. (3), the second-order coupling constants are expressed as[14]

$$a^{(2)}_{\mathbf{q}\nu;\mathbf{q}\nu} = \frac{1}{2} \Big[\mathbf{F}_{\mathbf{q}\nu} u^*_{\mathbf{q}\nu} u_{\mathbf{q}\nu} + \mathbf{D}_{\mathbf{q}\nu} u^*_{\mathbf{q}\nu} u_{\mathbf{q}\nu} \Big], \tag{4}$$

where $\mathbf{F}_{\mathbf{q}\nu} = \frac{1}{2}[\langle \psi^{(1)}_{\mathbf{k},\mathbf{q},n} | \hat{H}^{(1)}_{\mathbf{k}+\mathbf{q},\mathbf{k}} | \psi^{(0)}_{\mathbf{k}n} \rangle + (c.c.)]$ is the Fan term of the periodic part of the electronic wavefunction $|\psi^{(0)}\rangle$ with Hamiltonian $\hat{H}$, $\hat{H}^{(1)}$ is the first-order change of the

Hamiltonian due to a lattice distortion arising from nuclear vibrations, and $|\psi^{(1)}\rangle$ is the corresponding first-order change in the wavefunction. $\mathbf{D}_{\mathbf{q}\nu} = \langle\psi^{(0)}_{\mathbf{k}n}|\hat{H}^{(2)}_{\mathbf{k}-\mathbf{q},\mathbf{k}+\mathbf{q}}|\psi^{(0)}_{\mathbf{k}n}\rangle$ is the Debye-Waller (DW) term arising from the second-order change of the Hamiltonian due to nuclear vibrations. Using the rigid-ion approximation to recast the DW term in terms of first-order matrix elements that are directly accessible through routine DFPT calculations, one obtains the so-called Allen-Heine-Cardona theory.[15,16] Part of the DW term is neglected in the process, hence the approximation. The part of the DW term neglected by the rigid-ion approximation has been found to be small in crystals[14] but crucial for molecules.[17] Thanks to this approximation, very fine BZ grids can be used to fully converge the results.[18] In the main manuscript, this approximation is referred to as *Allen-Heine-Cardona theory* (AHC).

To obtain the finite displacement formulation of Eq. (3), the second-order coupling constants are expressed as

$$a^{(2)}_{\mathbf{q}\nu;\mathbf{q}\nu} = \frac{\epsilon_{\mathbf{k}n}(u_{\mathbf{q}\nu}) + \epsilon_{\mathbf{k}n}(-u_{\mathbf{q}\nu})}{2u^2_{\mathbf{q}\nu}}, \tag{5}$$

and explicit atomic displacements $\pm u_{\mathbf{q}\nu}$ are used to evalute the changes in the electronic eigenenergies. The finite displacement formulation does not rely on the rigid-ion approximation, but the vibrational BZ can only be sampled by explicitly constructing supercells of the primitive cell. Until recently, the fine BZ grids needed to converge the evaluation of electron-phonon coupling in this context made the calculations using the finite displacement method prohibitive, due to the large supercell sizes required. This situation has improved significantly thanks to the introduction of nondiagonal supercells, that provide access to very fine BZ grids using moderate supercells sizes, and approaching the levels of convergence available using DFPT.[10] In the main manuscript, this approximation is referred to as *finite displacements* (FD).

Despite the successes of the quadratic theory (AHC or FD) to describe the temperature dependence of the band structures of a range of materials, recent calculations question the validity of the AHC theory in helium at terapascal pressures,[19] molecular crystals at ambient conditions,[20] in the perovskite $CsSnI_3$,[21] and even (albeit moderately) in crystals

like diamond[22] because higher-order terms in the expansion of Eq. (2) make significant contributions. These terms can be included by evaluating Eq. (1) directly using Monte Carlo integration

$$\epsilon_{\mathbf{k}n}(T) \simeq \frac{1}{M}\sum_{i=1}^{M}\epsilon_{\mathbf{k}n}(\mathbf{u}_i), \tag{6}$$

where M is the number of sampling points, distributed according to the vibrational density. The use of Monte Carlo integration leads to statistical error bars in the Monte Carlo estimates of the integrals, which are given by

$$\delta\epsilon_{\mathbf{k}n}(T) \simeq \left[\frac{1}{M(M-1)}\sum_{i=1}^{M}\left(\epsilon_{\mathbf{k}n}(\mathbf{u}_i) - \frac{1}{M}\sum_{j=1}^{M}\epsilon_{\mathbf{k}n}(\mathbf{u}_j)\right)^2\right]^{1/2}. \tag{7}$$

Error bars are included in all results obtained using Monte Carlo integration, and if they cannot be seen in a given plot, that means that their size is smaller than the size of the point shown.

We emphasize here that the vibrational wave function is treated within the harmonic approximation, even when the higher order terms are included in the description of the coupling of vibrations to electronic eigenstates. Within the harmonic approximation, the vibrational density at temperature T is given by a product of Gaussian functions over the normal modes $\prod_{\mathbf{q},\nu}(2\pi\sigma^2_{\mathbf{q}\nu})^{-1/2}\exp(-\frac{u^2_{\mathbf{q}\nu}}{2\sigma^2_{\mathbf{q}\nu}})$ of amplitude

$$\sigma^2_{\mathbf{q}\nu}(T) = \frac{1}{\omega_{\mathbf{q}\nu}}\coth\left(\frac{\omega_{\mathbf{q}\nu}}{k_{\mathrm{B}}T}\right), \tag{8}$$

where k_{B} is Boltzmann's constant. While this approach fully accounts for all higher-order terms in electron-phonon coupling, the presence of cross-terms between different modes means that it cannot be used with DFPT or nondiagonal supercells, and therefore the computational advantages that these methods provide cannot be exploited. In the main manuscript, this approach is refereed to as the *Monte Carlo approach* (MC).

In Fig. 1 we compare the temperature dependence of the band gap of $MAPbI_3$ using the

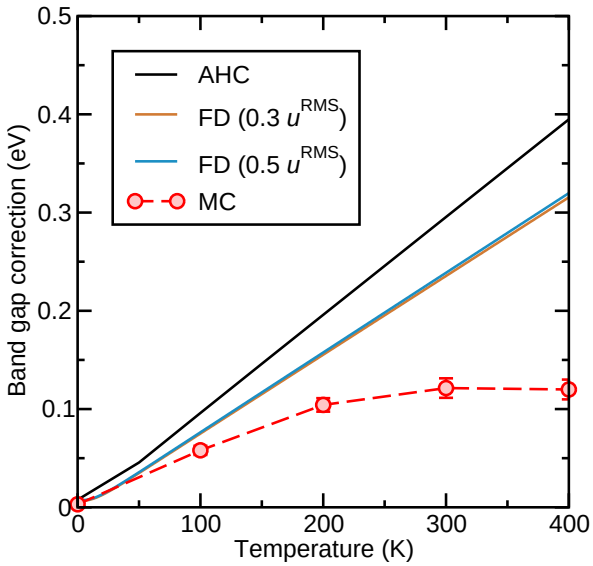

Figure 1: Temperature dependence of the band gap of $MAPbI_3$ evaluated using the AHC theory within DFPT (black lines), the quadratic approximation within a FD approach (blue and orange lines), and the MC sampling approach (red circles). For the FD approach, two sets of calculations have been performed, with finite displacement amplitudes given by $0.3u^{\mathrm{RMS}}$ and $0.5u^{\mathrm{RMS}}$ where $u^{\mathrm{RMS}} = \sqrt{\langle u^2 \rangle}$. The calculations have been performed by sampling a $2 \times 2 \times 2$ vibrational Brillouin zone grid, and without spin-orbit coupling. The statistical error bars in the MC results are included, but for the low temperature data points their size is smaller than the symbol size.

three different methods described above. The two approaches based on the quadratic expansion of Eq. (2), AHC and FD, show a significant increase in the value of the band gap with temperature, reaching 0.3-0.4 eV at 400 K. The disagreement between the two quadratic methods approaches 70 meV at 400 K. The origin of this discrepancy could be attributed to various factors. First, the AHC calculations have been performed with the ABINIT package,[11] while the FD calculations have been performed with the VASP package.[1–4] Different pseudopotentials and slightly different atomic coordinates have been used (although the volumes were the same). Given the above-mentioned differences, the agreement between the two methods is quite satisfactory. This leads us to believe that the rigid-ion approximation involved in the AHC approach seems to hold for molecular crystals. A more throughout investigation would be required to confirm this.

In any case, Fig. 1 clearly shows that the quadratic methods are not appropriate for the description of electron-phonon coupling in $MAPbI_3$, as they significantly overestimate the strength of the electron-phonon coupling. The higher-order terms included in the MC approach lead to a different temperature dependence of the band gap, and as shown in the main manuscript, agreement with experiment is only obtained if these higher-order terms are included.

Electronic structure method

In the main manuscript, we have established that the inclusion of SOC is necessary for an accurate description of the strength of the electron-phonon coupling in $MAPbI_3$, but that nonlocal electronic correlations are not important. Here, we provide further details of those calculations.

In evaluating Eq. (1), both electronic states and phonons are usually treated within semilocal DFT. However, semilocal DFT is known to severely underestimate band gaps in semiconductors and insulators.[23,24] In $MAPbI_3$, the situation is somewhat complex. The

experimental band gap is 1.6 eV,[25] and semilocal DFT predicts a band gap of about 1.6 eV,[26] which appears to be in good agreement with experiment. Nevertheless, the presence of Pb atoms means that SOC is strong in $MAPbI_3$, and its inclusion in the calculations reduces the band gap by around 1.0 eV,[27] so that indeed semilocal DFT underestimates the band gap. Performing calculations using hybrid functionals including SOC brings the gap closer to the experimental value, and GW+SOC calculations lead to band gaps in very good agreement with experiment.[28–30] It had been assumed for some time that, while electronic states were poorly reproduced by semilocal DFT, electron-phonon coupling was well-described by this level of theory, as only *changes* in band gaps need to be calculated. However, it has recently been shown that in some materials semilocal DFT severely underestimates the strength of electron-phonon coupling.[31,32]

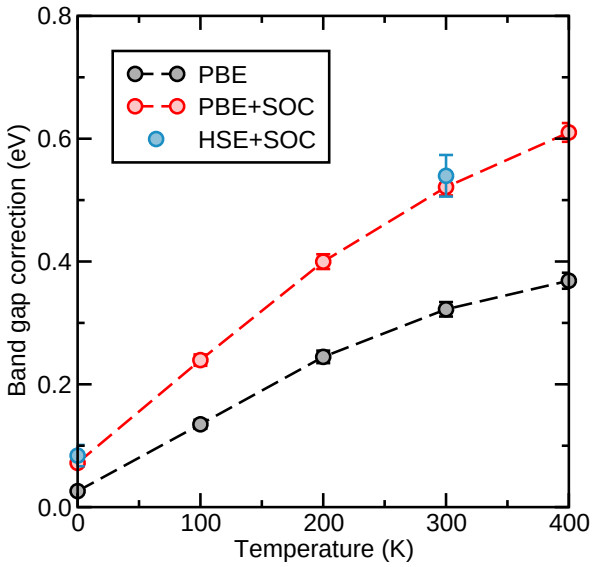

Figure 2: Temperature dependence of the band gap of $MAPbI_3$ evaluated using PBE (black circles), PBE+SOC (red circles), and HSE+SOC (blue circles), and the MC method. Only the electron-phonon coupling constants for $\mathbf{\Gamma}$-point phonons are included. The statistical error bars are included in all data points, although they are not visible in some as their size is smaller than the symbol size.

Using MC sampling, we evaluate the temperature dependence of the band gap of $MAPbI_3$ using PBE, PBE+SOC, and HSE+SOC, by focusing again on the $\mathbf{\Gamma}$-point phonons. The results are shown in Fig. 2. The inclusion of SOC significantly increases the strength of the

electron-phonon coupling, such that at 500 K, the band gap change is underestimated by 0.28 eV if the SOC is neglected. The effects of SOC arise exclusively from the CBM, which is mostly of Pb character. For example, at 300 K, the change in the VBM is −0.24 eV both without and with SOC, but the change in the CBM is +0.08 eV without SOC, and increases to +0.28 eV with SOC.

The use of the hybrid functional HSE[6,7] instead of PBE does not seem to make a significant difference. As a consequence, the final results in the main manuscript are obtained using PBE+SOC.

Brillouin zone sampling

Using the quadratic theory of Eq. (3), it has been shown that the strength of electron-phonon coupling converges slowly as a function of vibrational BZ grid size.[10,18] Unfortunately, the quadratic theory is not applicable to $MAPbI_3$ due to the importance of high-order terms, and that the methods developed to accurately sample the BZ cannot be used here. For the MC sampling method, supercells of the primitive cell need to be constructed, and their sizes are limited by the maximum number of atoms that can be realistically included in a DFT calculation. In our case, we find that we can reach system sizes of $3 \times 3 \times 3$ primitive cells, containing 324 atoms.

In Fig. 3 we show the temperature dependence of the band gap of $MAPbI_3$ for supercells of varying sizes, and it is clear that the band gap change is not converged for the largest supercells studied. Nonetheless, the changes arising from using supercells of varying size are smaller than either the changes induced by including higher-order terms or the SOC interaction. Furthermore, the change in the band gap at the relevant temperatures for solar cell applications, of above 300 K, is similar between the $2 \times 2 \times 2$ and the $3 \times 3 \times 3$ supercells, and the difference is smaller than the experimental uncertainty in the available data. Therefore, our final results in the main manuscript are reported for the $3 \times 3 \times 3$

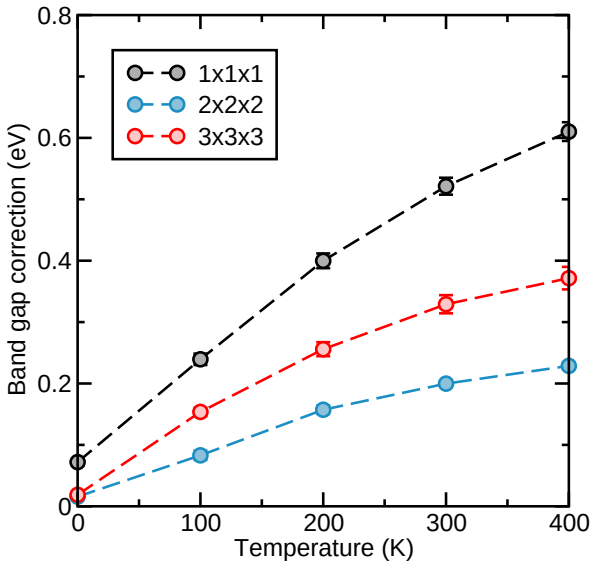

Figure 3: Temperature dependence of the band gap of $MAPbI_3$ evaluated using supercells of sizes $1 \times 1 \times 1$ (black circles), $2 \times 2 \times 2$ (blue circles), and $3 \times 3 \times 3$ (red circles). The statistical error bars are included in all data points, although they are not visible in some as their size is smaller than the symbol size.

supercell.

Results using the AHC theory and MC sampling

In this section we describe several results obtained using the AHC theory and MC sampling. In Fig. 4 we show the static lattice band structure of $MAPbI_3$ calculated using the PBE functional without the inclusion of SOC. The values of several band gaps from the valence band maximum (VBM) at the $\mathbf{R} = (0.5, 0.5, 0.5)$ point to the conduction band of several high-symmetry points are indicated by the arrows. The conduction band minimum (CBM) is also located at the $\mathbf{R}$ point. In Fig. 5 we show the temperature dependence of these band gaps, calculated using the AHC theory with a $20 \times 20 \times 20$ BZ sampling. The different changes with temperature exhibited by the different gaps indicate that temperature does not only change the absolute value of the band gaps, but also changes the shape of the band structure. Fig. 5 also shows the temperature dependence of the individual eigenvalues at the valence and conduction bands at several high-symmetry points in the vibrational BZ. For

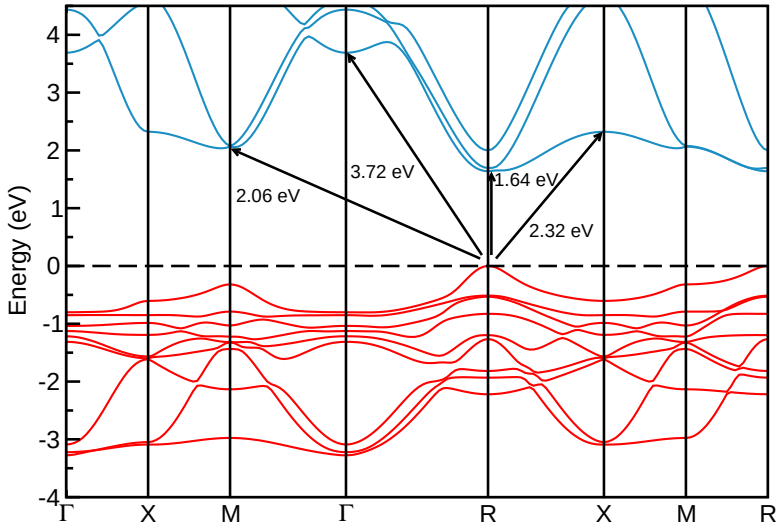

Figure 4: Static lattice band structure of $MAPbI_3$ calculated using the PBE functional without including SOC. The dashed line indicates the position of the Fermi level.

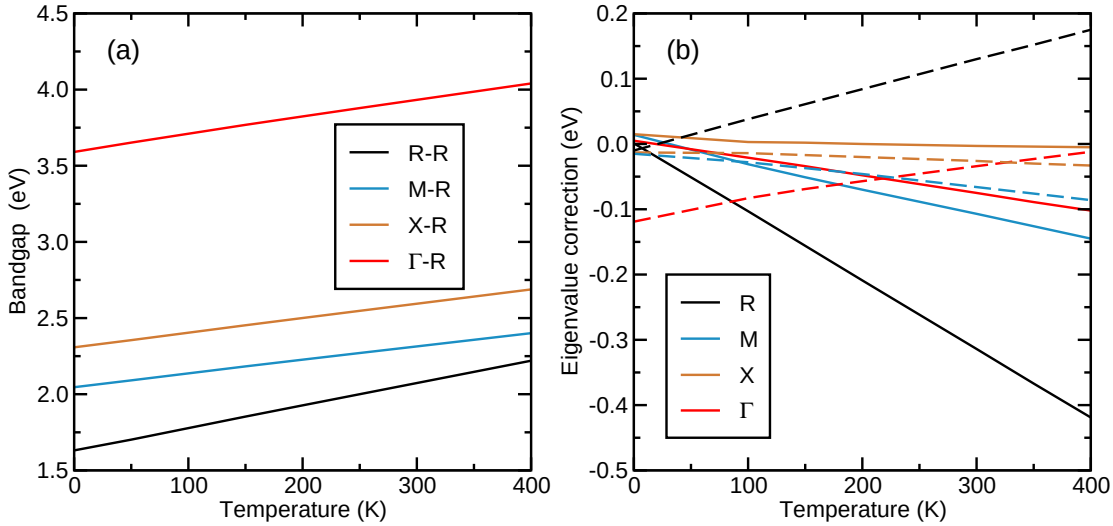

Figure 5: (a) Temperature dependence of band gaps of $MAPbI_3$ from the VBM at the **R** point to the conduction band of several high-symmetry points in the BZ. (b) Temperature dependence of the individual eigenvalues at the valence (solid lines) and conduction (dashed lines) band at several high-symmetry points of the BZ. All calculations have been performed using the PBE functional and the AHC theory. The SOC and thermal expansion are not included.

the minimum band gap at **R** discussed in the main text, the VBM decreases with increasing temperature, and the CBM increases with increasing temperature.

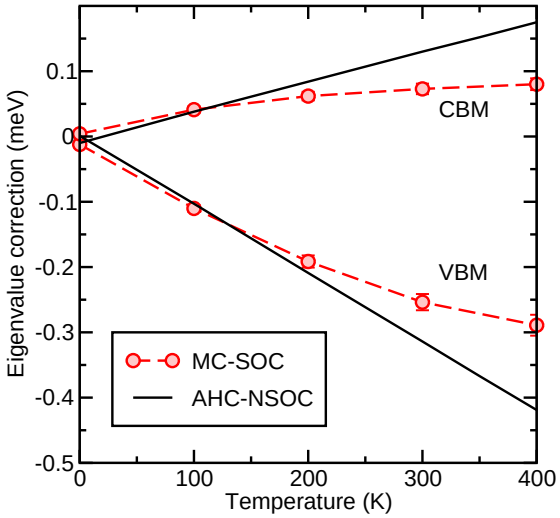

Figure 6: Temperature dependence of the individual eigenvalues at the valence (lower lines) and conduction (upper lines) band at the **R**-point of the BZ. The calculations have been performed using the same numerical parameters as those in Fig. 3 of the main manuscript, but without the inclusion of thermal expansion.

In Fig. 6 we show the temperature dependence of the VBM and CBM at the **R** point using MC sampling with the PBE+SOC method, and a supercell of size $3 \times 3 \times 3$, numerical parameters corresponding to the final results presented in the main manuscript. For comparison, we also repeat the results arising from using the AHC theory. These calculations do not include the effects of thermal expansion, as a proper treatment of the average electrostatic potential in simulation cells of varying volumes would be required, but this is beyond the scope of the present work. The results in Fig. 6 show that the use of MC sampling corrects to a large extent the defficiencies of the AHC approach, by almost removing the temperature dependence of the CBM at temperatures above 290 K, of experimental interest. The results in Ref.[33] suggest that the inclusion of thermal expansion would make the temperature dependence of the CBM negative, in agreement with the experimental observations.

Thermal expansion

We study thermal expansion within the quasiharmonic approximation. The Helmholtz free energy of a solid at temperature T can be written as

$$\mathcal{F}(V,T) = \mathcal{U}(V,T) + E_{\text{vib}}(V,T), \tag{9}$$

where V is the volume, $\mathcal{U}$ is the electronic energy, and E_{vib} represent the vibrational energy. For systems with a band gap, $\mathcal{U}(V,T) \approx \mathcal{U}(V)$. The equilibrium volume at temperature T is determined by minimizing $\mathcal{F}(V,T)$, which we do by calculating the vibrational energy within the harmonic approximation at a range of volumes and then directly minimizing $\mathcal{F}(V,T)$.

The calculations have been performed using density functional theory (DFT) together with the Tkatchenko-Scheffler van der Waals scheme.[34] Using this approach, we find that the lattice constant at zero temperature of 6.37 Å increases to 6.40 Å at 300 K, which is in good agreement with experiment.[35]

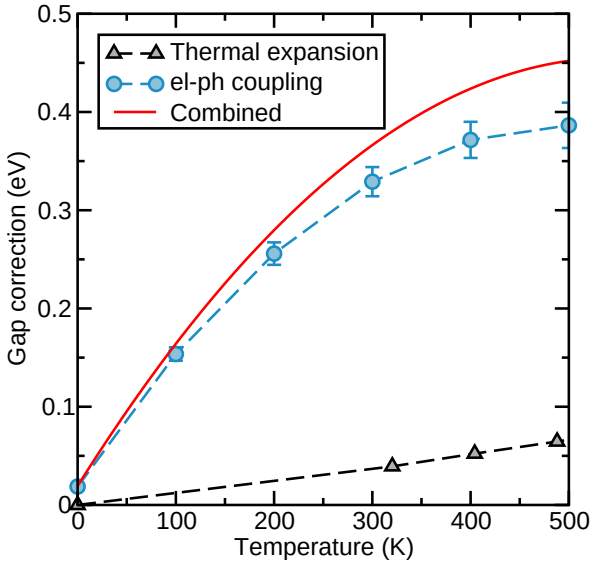

Figure 7: Temperature dependence of the band gap of $MAPbI_3$ evaluated using thermal expansion only (black triangles), electron-phonon coupling only with MC and SOC on a $3 \times 3 \times 3$ supercell (blue circles), and both (red dashed-dotted line). The statistical error bars are included in all MC data points, although they are not visible in some as their size is smaller than the symbol size.

The change in the band gap due to thermal expansion is shown in Fig. 7, where it is compared with the electron-phonon coupling induced change. Electron-phonon coupling makes the largest contribution, with a band gap opening of about 0.40 eV at 500 K, compared to 0.07 eV for thermal expansion.

$CsPbI_3$

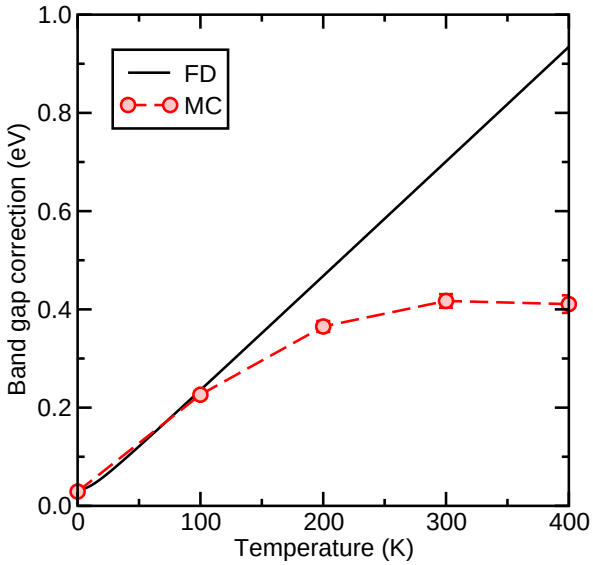

Figure 8: Temperature dependence of the band gap of $CsPbI_3$ evaluated using the FD and MC methods. The calculations have been performed using the PBE functional, with a $2 \times 2 \times 2$ BZ grid, and without including SOC. Statistical error bars are included in the MC data points, but they are not visible for some data points as they are smaller than the symbols.

In Fig. 8 we show the temperature dependence of the band gap of $CsPbI_3$ evaluated using the quadratic approximation within the FD approach, and also using MC sampling. The calculations correspond to a sampling of the BZ with a grid of size $2\times2\times2$ and do not include SOC. As observed for $MAPbI_3$ in the main manuscript, high-order terms in the electron-phonon coupling are also necessary to accurately describe the temperature dependence of $CsPbI_3$.

References

(1) Kresse, G.; Hafner, J. *Ab initio* molecular dynamics for liquid metals. *Phys. Rev. B* **1993**, *47*, 558.

(2) Kresse, G.; Hafner, J. *Ab initio* molecular-dynamics simulation of the liquid-metal-amorphous-semiconductor transition in germanium. *Phys. Rev. B* **1994**, *49*, 14251.

(3) Kresse, G.; Furthmüller, J. Efficiency of ab-initio total energy calculations for metals and semiconductors using a plane-wave basis set. *Comput. Mater. Sci.* **1996**, *6*, 15.

(4) Kresse, G.; Furthmüller, J. Efficient iterative schemes for *ab initio* total-energy calculations using a plane-wave basis set. *Phys. Rev. B* **1996**, *54*, 11169.

(5) Perdew, J. P.; Burke, K.; Ernzerhof, M. Generalized Gradient Approximation Made Simple. *Phys. Rev. Lett.* **1996**, *77*, 3865.

(6) Paier, J.; Marsman, M.; Hummer, K.; Kresse, G.; Gerber, I. C.; Ángyán, J. G. Screened hybrid density functionals applied to solids. *J. Chem. Phys.* **2006**, *124*, 154709.

(7) Paier, J.; Marsman, M.; Hummer, K.; Kresse, G.; Gerber, I. C.; Ángyán, J. G. Erratum: Screened hybrid density functionals applied to solids [J. Chem. Phys. 124, 154709 (2006)]. *J. Chem. Phys.* **2006**, *125*, 249901.

(8) Blöchl, P. E. Projector augmented-wave method. *Phys. Rev. B* **1994**, *50*, 17953.

(9) Kresse, G.; Joubert, D. From ultrasoft pseudopotentials to the projector augmented-wave method. *Phys. Rev. B* **1999**, *59*, 1758.

(10) Lloyd-Williams, J. H.; Monserrat, B. Lattice dynamics and electron-phonon coupling calculations using nondiagonal supercells. *Phys. Rev. B* **2015**, *92*, 184301.

(11) Gonze, X.; Jollet, F.; Araujo, F. A.; Adams, D.; Amadon, B.; Applencourt, T.; Audouze, C.; Beuken, J.-M.; Bieder, J.; Bokhanchuk, A. et al. Recent developments in the ABINIT software package. *Comput. Phys. Comm.* **2016**, *205*, 106.

(12) Gonze, X.; Lee, C. Dynamical matrices, Born effective charges, dielectric permittivity tensors, and interatomic force constants from density-functional perturbation theory. *Phys. Rev. B* **1997**, *55*, 10355.

(13) Kunc, K.; Martin, R. M. *Ab Initio* Force Constants of GaAs: A New Approach to Calculation of Phonons and Dielectric Properties. *Phys. Rev. Lett.* **1982**, *48*, 406.

(14) Poncé, S.; Antonius, G.; Gillet, Y.; Boulanger, P.; Laflamme Janssen, J.; Marini, A.; Côté, M.; Gonze, X. Temperature dependence of electronic eigenenergies in the adiabatic harmonic approximation. *Phys. Rev. B* **2014**, *90*, 214304.

(15) Allen, P. B.; Heine, V. Theory of the temperature dependence of electronic band structures. *J. Phys. C* **1976**, *9*, 2305.

(16) Allen, P. B.; Cardona, M. Theory of the temperature dependence of the direct gap of germanium. *Phys. Rev. B* **1981**, *23*, 1495.

(17) Gonze, X.; Boulanger, P.; Côté, M. Theoretical approaches to the temperature and zero-point motion effects on the electronic band structure. *Ann. Phys.* **2011**, *523*, 168–178.

(18) Poncé, S.; Gillet, Y.; Laflamme Janssen, J.; Marini, A.; Verstraete, M.; Gonze, X. Temperature dependence of the electronic structure of semiconductors and insulators. *J. Chem. Phys.* **2015**, *143*, 102813.

(19) Monserrat, B.; Drummond, N. D.; Pickard, C. J.; Needs, R. J. Electron-Phonon Coupling and the Metallization of Solid Helium at Terapascal Pressures. *Phys. Rev. Lett.* **2014**, *112*, 055504.

(20) Monserrat, B.; Engel, E. A.; Needs, R. J. Giant electron-phonon interactions in molecular crystals and the importance of nonquadratic coupling. *Phys. Rev. B* **2015**, *92*, 140302.

(21) Patrick, C. E.; Jacobsen, K. W.; Thygesen, K. S. Anharmonic stabilization and band gap renormalization in the perovskite $CsSnI_3$. *Phys. Rev. B* **2015**, *92*, 201205.

(22) Antonius, G.; Poncé, S.; Lantagne-Hurtubise, E.; Auclair, G.; Gonze, X.; Côté, M. Dynamical and anharmonic effects on the electron-phonon coupling and the zero-point renormalization of the electronic structure. *Phys. Rev. B* **2015**, *92*, 085137.

(23) Godby, R. W.; Schlüter, M.; Sham, L. J. Accurate Exchange-Correlation Potential for Silicon and Its Discontinuity on Addition of an Electron. *Phys. Rev. Lett.* **1986**, *56*, 2415–2418.

(24) Godby, R. W.; Schlüter, M.; Sham, L. J. Self-energy operators and exchange-correlation potentials in semiconductors. *Phys. Rev. B* **1988**, *37*, 10159–10175.

(25) Baikie, T.; Fang, Y.; Kadro, J. M.; Schreyer, M.; Wei, F.; Mhaisalkar, S. G.; Grätzel, M.; White, T. J. Synthesis and crystal chemistry of the hybrid perovskite $(CH_3NH_3)PbI_3$ for solid-state sensitised solar cell applications. *J. Mater. Chem. A* **2013**, *1*, 5628.

(26) Brivio, F.; Walker, A. B.; Walsh, A. Structural and electronic properties of hybrid perovskites for high-efficiency thin-film photovoltaics from first-principles. *APL Mater.* **2013**, *1*, 042111.

(27) Even, J.; Pedesseau, L.; Jancu, J.-M.; Katan, C. Importance of Spin-Orbit Coupling in Hybrid Organic/Inorganic Perovskites for Photovoltaic Applications. *J. Phys. Chem. Lett.* **2013**, *4*, 2999.

(28) Umari, P.; Mosconi, E.; De Angelis, F. Relativistic *GW* calculations on $CH_3NH_3PbI_3$ and $CH_3NH_3SnI_3$ Perovskites for Solar Cell Applications. *Sci. Rep.* **2014**, *4*, 4467.

(29) Brivio, F.; Butler, K. T.; Walsh, A.; van Schilfgaarde, M. Relativistic quasiparticle self-consistent electronic structure of hybrid halide perovskite photovoltaic absorbers. *Phys. Rev. B* **2014**, *89*, 155204.

(30) Filip, M. R.; Giustino, F. *GW* quasiparticle band gap of the hybrid organic-inorganic perovskite $CH_3NH_3PbI_3$: Effect of spin-orbit interaction, semicore electrons, and self-consistency. *Phys. Rev. B* **2014**, *90*, 245145.

(31) Antonius, G.; Poncé, S.; Boulanger, P.; Côté, M.; Gonze, X. Many-Body Effects on the Zero-Point Renormalization of the Band Structure. *Phys. Rev. Lett.* **2014**, *112*, 215501.

(32) Monserrat, B. Correlation effects on electron-phonon coupling in semiconductors: Many-body theory along thermal lines. *Phys. Rev. B* **2016**, *93*, 100301.

(33) Foley, B. J.; Marlowe, D. L.; Sun, K.; Saidi, W. A.; Scudiero, L.; Gupta, M. C.; Choi, J. J. Temperature dependent energy levels of methylammonium lead iodide perovskite. *Appl. Phys. Lett.* **2015**, *106*, 243904.

(34) Tkatchenko, A.; Scheffler, M. Accurate Molecular Van Der Waals Interactions from Ground-State Electron Density and Free-Atom Reference Data. *Phys. Rev. Lett.* **2009**, *102*, 073005.

(35) Saidi, W. A.; Choi, J. J. Nature of the Cubic to Tetragonal Phase Transition in Methylammonium Lead Iodide Perovskite. *The Journal of Chemical Physics* **2016**, in press.